Analysis of Dynamic Data from Supersonic Retropropulsion Experiments in NASA Langley's Unitary Plan Wind Tunnel

Joshua R. Codoni[1]
Department of Mechanical and Aerospace Engineering, University of Virginia, Charlottesville, VA, 22903

Scott A. Berry[2]
NASA Langley Research Center, Hampton, VA 23681

Recent experimental supersonic retropropulsion tests were conducted at the NASA Langley Research Center Unitary Plan Wind Tunnel Test Section 2 for a range of Mach numbers from 2.4 to 4.6. A 5-inch 70-degree sphere-cone forebody model with a 10-inch cylindrical aftbody experimental model was used which is capable of multiple retrorocket configurations. These configurations include a single central nozzle on the center point of the forebody, three nozzles at the forebody half-radius, and a combination of the first two configurations with no jets being plugged. A series of measurements were achieved through various instrumentation including forebody and aftbody pressure, internal pressures and temperatures, and high speed Schlieren visualization. Specifically, several high speed pressure transducers on the forebody and in the plenum were implemented to look at unsteady flow effects. The following work focuses on analyzing frequency traits due to the unsteady flow for a range of thrust coefficients for single, tri, and quad-nozzle test cases at freestream Mach 4.6 and angle of attack ranging from -8° to +20°. This analysis uses Matlab's fast Fourier transform, Welch's method (modified average of a periodogram), to create a power spectral density and analyze any high speed pressure transducer frequency traits due to the unsteady flow.

Nomenclature

M	= Mach number	b	= angle of yaw, deg
Re	= Reynolds number	A_{Ref}	= area reference, in^2
T	= temperature, deg-F or deg-R	f	= model roll, deg
P	= pressure, psia or psf	r, q	= model polar coordinates
q	= dynamic pressure, psf		
C_T	= thrust coefficient		
T^*	= thrust, lbf	*Subscripts:*	
x, y, z	= model coordinate system, in	T	= stagnation or total conditions
X, Y, Z	= tunnel coordinate system, in	∞	= freestream conditions
a	= angle of attack, deg	j	= jet conditions

I. Introduction

[1] Graduate Student, Student Member AIAA.
[2] Aerospace Engineer, Aerothermodynamics Branch, M/S 408a, AIAA Associate Fellow.

ENTRY, descent, and landing (EDL) is one of many challenging aspects of Mars missions. The variable, relatively low atmospheric density is sufficient enough to cause substantial heating, but insufficient for adequately decelerating future proposed missions. Current EDL technology is a remnant from the Viking-era and includes the standard 70 degree sphere-cone blunt body, an ablative thermal protection system (TPS) and supersonic parachutes. However, the limits of this technology are quickly being approached as the desire to land heavier mass systems at a wider range of locations increases.[1] A major challenge to the EDL portion of Mars missions is adequately decelerating a lander to a safe speed prior to touchdown. Expanding parachute size and increasing the operating range to higher speeds is desirable, but these changes only offer marginal benefits and more research and development would be necessary. In order to obtain adequate decelerating capabilities for proposed future manned missions, which would need landed masses at least an order of magnitude larger than current capabilities, it will be necessary to research and develop alternative means; for more discussion on the current limitations and possible improvements as well as systems studies, see Ref. 2,3,4 & 5.

One such alternative to improve landing capabilities is retropropulsion initiated in the supersonic stages of flight. Supersonic retropropulsion (SRP) involves using rocket(s) thrust opposite the direction of motion to further slow the landing vehicle. Previous experimental data[6,7] from the late 1960s and early 1970s developed a useful foundation for understanding the aerodynamics associated with such a flow, shown notionally in Fig. 1. As thrust is initiated at supersonic conditions, for a single central case, the bow shock is pushed away from the aeroshell. A free stagnation point forms between the jet barrel shock and bow shock and recirculation regions are created near the shoulder of the aeroshell. However in order to mature the technology to an adequate level of usefulness for Mars missions it is necessary to further investigate the highly complex flow-field through experimentation to provide high fidelity comparisons with computational code, such as Ref. 8. Historical data indicated certain flow-field conditions would be unsteady. Thus, the experiment was designed with high-speed instrumentation, both Schlieren and dynamic pressure transducers to provide an adequate measure of the unsteadiness for comparison against computational fluid dynamic (CFD) code.

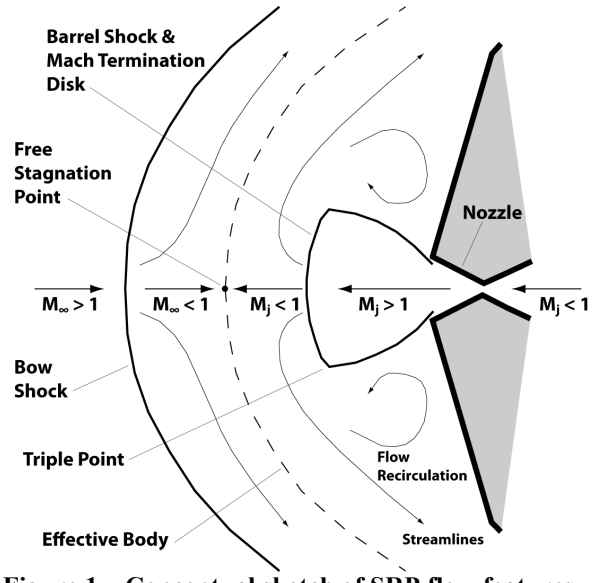

Figure 1 – Conceptual sketch of SRP flow features

II. Experimental Setup

The experiment for this study was conducted at the NASA Langley Research Center Unitary Plan Wind Tunnel (LaRC UPWT). The NASA LaRC UPWT is a closed-circuit continuous flow pressure tunnel with two test sections that are nominally 7 feet long and 4-ft by 4-ft in cross section. Test section 2 was used exclusively for this study under the conditions listed in Table 1. A range of thrust coefficients ($C_T=T^*/q_\infty A_{ref}$, where T^* is the total thrust, q_∞ is freestream dynamic pressure, and A_{ref} is a reference area) were tested for multiple model configurations based on priority and availability due to tunnel limitations.

Table 1. Nominal UPWT test section 2 flow conditions

M_∞	Re_∞ (1/ft)	$T_{T\infty}$ (deg-R)	$P_{T\infty}$ (psf)	P_∞ (psf)	q_∞ (psf)
2.4	1.0E+06	610	814.9	55.7	224.7
3.5	1.0E+06	610	1485.8	19.5	167.0
4.6	1.5E+06	610	3922.1	12.0	177.3

Standard Test Section 2 model mounting hardware was utilized for this test, as shown in Figure 2. The basic mechanism is a horizontal wall-mounted strut capable of forward and aft travel (in the X-direction) of 36.25 in. Attached to this strut is a sting support which allows left/right traversal (in the Y-direction) of ±20 in. and sideslip angle (β) of up to ±14-deg. Forward of the sting support are the angle-of-attack (α) and roll

mechanisms, which for this study provided pitch angles from -8 to 20-deg and roll angles from 0 to 180-deg. The large tunnel size and mounting hardware for the UPWT were ideal for acquiring uncertainty estimation data[9], as random and bias uncertainties can be assessed by moving and rolling the model to provide sensor-to-sensor repeatability and measurements of flow-field nonuniformity.

A. Model Design and Instrumentation

An oblique view of the SRP model design is shown in Fig. 3, a 5-in diameter highly-instrumented 70-deg sphere-cone forebody with locations for 4 nozzle or plug inserts followed by a cylindrical aftbody. The assembled model was designed with a partially hollow sting, as shown in cutaway sketch of Figure 4, that feeds an internal plenum connected to each nozzle location via a four-fingered manifold. Note that the plenum is a constant diameter pipe with a 5-deg flare leading to the manifold. The predicted Mach number within the plenum is approximately 0.1 at worst-case conditions. The sting/plenum/manifold assembly provides the structural load path to hold the forebody with either plugs or nozzles in place. The 9.55-in long aftbody, comprised of two thin-walled half cylinders, provides an enclosure to protect internal instrumentation (also shown in Fig. 4) and carries no load. Nozzle locations include one on model centerline and three on the forebody half-radius spaced 120° apart. The insert locations can host either 4:1 exit-to-throat area ratio nozzles or plugs that fit flush to the forebody, providing the baseline configuration. Configuration changes are handled by removing one side panel and sliding the forebody forward (without disconnecting the ports) to replace the inserts.

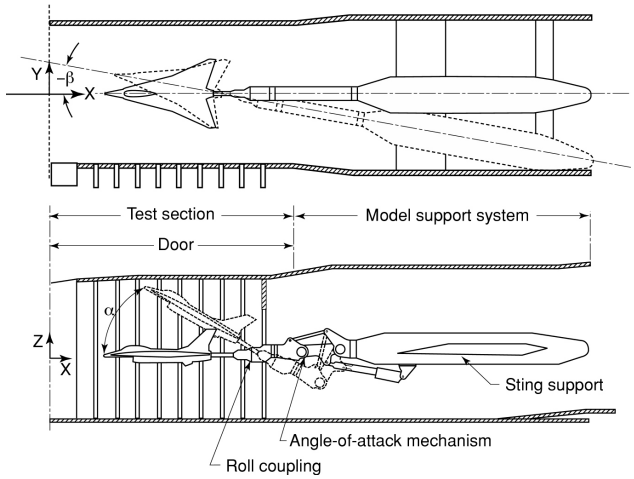

Figure 2 – Test section 2 model support system and coordinate system

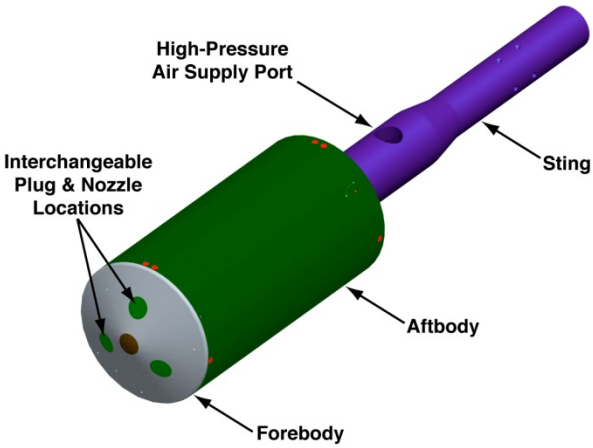

Figure 3 – Oblique view of UPWT SRP model assembly

A full array of instrumentation was used to provide surface pressure, pitch and angle, plenum pressure and temperature, and nozzle mass flow rate. This instrumentation included: surface pressure ports connected to Pressure

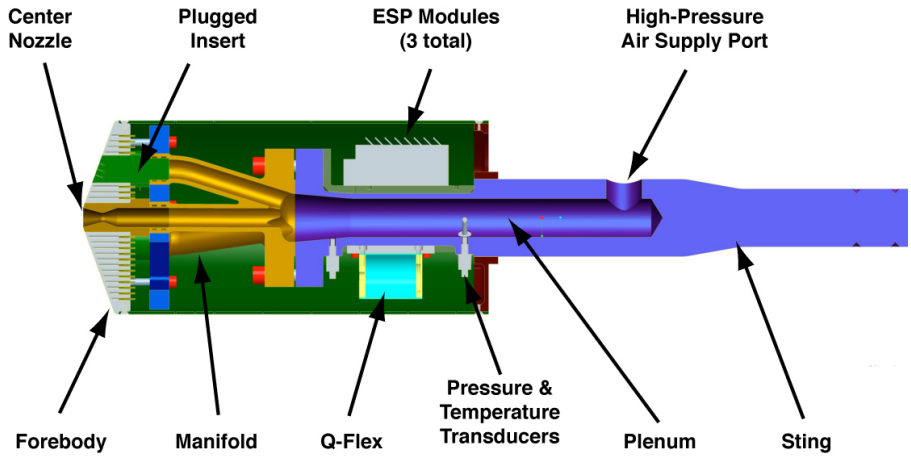

Figure 4 – Section view of the final design UPWT SRP model assembly

Systems Inc (PSI) electronically scanned pressure (ESP) transducer modules sampled at 10 Hz, Kulite XCS-062-5A pressure transducers sampled at 40 kHz as well as averaged, a NASA Langley-built Q-Flex accelerometer, type J and K thermocouples, and a Flow-Dyne Engineering subsonic venturi flow meter. For a full discussion of all of the instrumentation as well as a more in-depth coverage of the experimental set-up, data acquisition, and test parameters, see Ref. 10 and 11.

III. Results

The present paper will focus on reporting a small subset of frequency traits from the unsteady analysis of the dynamic pressure measurements; the total set of data, including all Schlieren and pressure results, will be included in an upcoming NASA report. The dynamic sensors were sampled at 40 kHz for a 2.5 second period using a National Instruments Labview-based high-speed data system synchronized to the standard data system. These data were processed through a 20 kHz low-pass filter and recorded at 16-bit A/D conversion. Each resulting data file had 81,920 data points (40K samples per second for 2.048 seconds). A power spectral density (PSD) analysis was performed using MatLab's fast Fourier transform (FFT) Welch method, which is a modified average of a periodogram. The data were broken into 80 blocks at 2048 samples per block with a 50% overlapping Hanning window which prevents aliasing of the results. This approach allowed for improved block averaging to reduce noise within the resulting analysis. The resulting frequency resolution using this approach is 19.53 Hz.

Figure 5 shows the location of all presssure ports, both steady (ESP) and dynamic (Kulite), on the forebody of the aeroshell at zero roll. Note Kulite P105 was damaged during the experiment. In this orientation, positive angle of attack would be in the upward directions such that the lower sensors (106, 107, and 108) would be on the windward side of the forebody. Four dynamic pressure sensors are also located at various locations within the model plenum. However, the internal unsteady analysis results are not presented here as any frequency dynamics detected in the plenum were due to different stagnation pressure conditions for varied C_T, and there was not found to be any correlation with forebody dynamics. Each run to be discussed subsequently utilized the same angle of attack sequence with the model first starting at $\alpha = -8°$ and pitching in the positive direction at 4° increments up to 20°, followed by an end-of-run repeat of the $\alpha = 0°$ case. Thus within each run, there are 9 test points with two at $\alpha = 0°$ and two each at $\alpha = \pm 4°$ and $\pm 8°$. The subsequent PSD results will be contained in figures, each to a page, at the end of the paper, and the AOA sequence reads from left to right, then top to bottom with alpha indicated in the title of each plot. The following discussion and results are for central, tri and quad-nozzle configuration test cases with a freestream Mach number of 4.6. Peaks of interest that will be discussed in the following sections will also be identified on the plots.

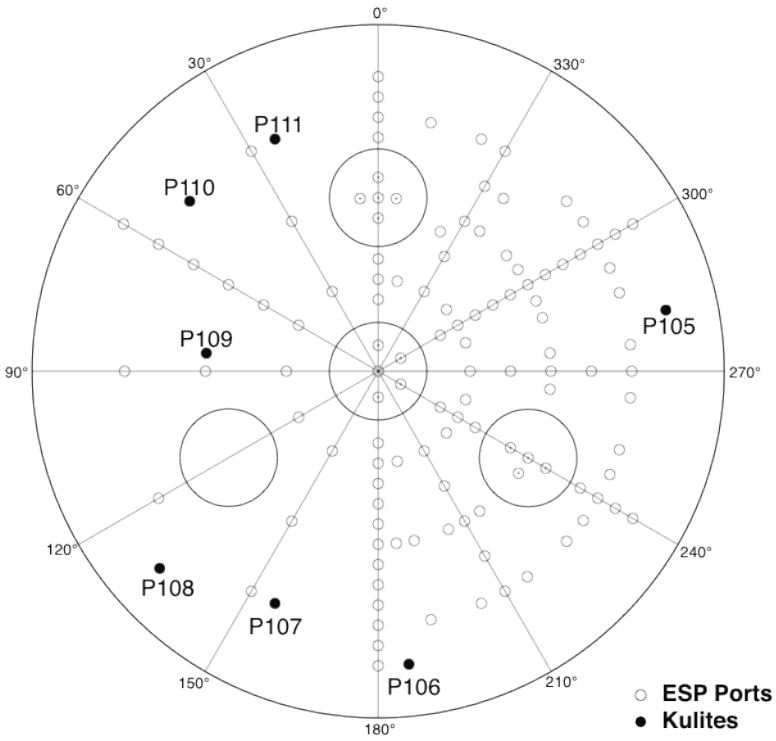

Figure 5 – Sketch showing forebody sensors locations for f = 0°

A. Single Central Nozzle

A single frame Schlieren image of the single-nozzle configuration for $\alpha = 0$ with $C_T = 0.94$ in Mach 4.6 freestream flow is shown in Figure 6. Freestream flow is from left to right, with the model supported from the right and retrorocket blowing towards the left of the image. The vertical bars in the image are from the facility optical access windows and are not part of the flow. The darker streaks on the lower, left of the image were due to an oil leak within the tunnel that provided occasional streaking along the window. These streaks were cleaned off the window each time the tunnel was shut down for a configuration change. Schlieren videos were used to record the unsteady nature of the flow and were shot at framing rates between 5,000 and 10,000 fps. It is difficult to capture the unsteady nature of the flow in a single frame image, and this is further discussed in Reference 11. However, the primary flow fluctuations from this case were seen at the so-called "triple-point" (identified in Fig. 1), which is an annular region formed at the junction of the Mach termination disk and barrel shock.

Figure 6 – Sample Schlieren result for center nozzle at Mach 4.6, $\alpha = 0°$, $\beta = 0°$, and $C_T = 0.94$

Figure 7, contained towards the end of the paper, provides the background frequency content on the forebody in the absence of nozzle thrusting for Run 174, which was a case where the center nozzle was installed but with no blowing. As can be seen in the series of plots for each test point (and thus angle of attack), with $C_T = 0$ there are no observable peaks of frequency that rise above the background noise. There is, however, a subtle angle of attack effect, with the windward and leeward sensors separating slightly as alpha increases. With the model at zero roll, the lower sensors (106, 107, and 108) are windward for positive angles of attack, which result in higher PSD curves than the rest (109, 110, and 111).

Figure 8, for Run 171, is with $C_T = 0.22$, which resulted in some measurable dynamics to be picked up at the surface of the forebody. Over most of the range of test points (TP), a peak at frequency near 1.5 kHz is observed to rise sharply above the noise. This primary frequency shows up on all six sensors and remains static for most of the alpha range, but does shift slightly at the higher angles of attack. Note that any frequency peaks that are observed to rise above the background noise levels (established from the no-blowing case already discussed) will be marked and identified on each plot as appropriate. A secondary peak becomes evident, mainly on the windward sensors, at angles of attack (AOA) of 8° and above providing frequencies that vary from 0.1 to 2.0 kHz.

Figure 9 (Run 170) is for $C_T = 0.46$, which provided for a different dynamic behavior than the lower C_T case, one in which multiple frequencies were measured that varied with each angle of attack. For the $\alpha = 0°$ case, there were two fairly strong peaks that were measured by all six sensors, one at 1.7 kHz and a double humped peak of 7.8 to 8.2 kHz. There were also a few minor peaks, at 3.9 and 5.4 kHz, which seemed most prominent on the sensors closest to the nozzle, particularly sensor 109 but also on 110, and 111. As angle of attack increased, the windward sensors indicate a slight shift to higher frequencies while the leeward sensors shift to lower. For the 4° AOA-pair (test points 2255 and 2257), the measured results are consistent with the windward sensors displaying the higher PSD curves and frequencies of roughly 1.8, 6.1 and 8.5 kHz. The leeward sensors are picking up frequencies 1.7, 5.2, and 7.5 kHz. For the 8° AOA-pair (2254 and 2258), both cases show minor peaks at roughly 2.2 to 2.3 kHz for windward sensors, but the negative AOA case also indicate higher frequencies on the windward side at 3.8 and 5.8 kHz that are not seen in the corresponding positive AOA case. The positive AOA case also has a small, broad peak at 1.3 kHz for the leeward sensors. Above $\alpha = 8°$, the windward sensors have peaks at frequencies ranging between 0.5 and 4.3 kHz, with a peak always near 0.5 to 0.8 kHz and 2.2 to 2.5 kHz. The largest peak, 4.3 kHz only becomes visible at $\alpha = 20°$. The leeward sensors pick up peaks that migrate with angle of attack: 1.3 kHz at $\alpha = 12°$, 1.4 kHz at $\alpha = 16°$, and 1.9 kHz at $\alpha = 20°$.

Figure 10 (Run 167) is for $C_T = 0.94$ and had similar trends to the previous discussion. For the alpha of zero case (TP 2229 and 2235), a fairly strong peak at 6.9 kHz was picked up by all six sensors, while somewhat smaller peaks at 2.8 and 4.8 kHz were also seen (these lower frequency peaks were most prominent with sensor 109, the one closest to the nozzle). As before, the ±4° AOA-pair indicated a shift to higher frequencies on the windward side,

while the leeward side shifted lower slightly. For the 8° AOA-pair, a single strong peak was observed at 2.1 kHz, and a small secondary peak at 4.8 kHz for the positive case. As the angle of attack increased further, this primary peak migrated to lower frequencies (1.1 kHz at 12 deg, 0.9 kHz at 16 deg, and 0.7 kHz at 20 deg), and in some case a secondary peak was observed (2.4 kHz at 16° and 2.3 kHz at 20°).

Figure 11 (Run 166) is for $C_T = 1.97$ and has the strongest and sharpest peaks seen thus far, as well as a different dynamic than noted for the previous two cases. There is a primary sharp peak at 2.2 kHz as well as harmonics at 4.4, 6.5, and 8.7 kHz. Further, sensor p109 has a small peak at 4.1 kHz, and all sensors detect a minor peak at roughly 0.8 kHz. The zero-repeat case (TP 2226) also has a sharp peak double peak at 2.0 and again at 2.2 kHz for all sensors. The small peak at roughly 4.1 kHz, which was only visible for the p109 sensor previously, is now visible for all the sensors at roughly 4.0 kHz and appears to be a harmonic of the 2.0 kHz peak. Unlike previous test cases, the ±4° AOA-pair shows windward sensors shifting to lower frequencies (compared to a zero AOA case) of 1.8-1.9 kHz and 3.7-3.8 kHz, while the leeward sensors shift to slightly higher frequencies of 2.2-2.3 kHz for. For the ±8° AOA-pair both windward and leeward sensors show a sharp peak, which still reduced in frequency from the initial zero-AOA cases, at 1.7 and 3.3-3.5 kHz as well as minor peaks at 0.4 and 5.7 kHz. As α increases to 12° and greater the major peaks continue to match up for both windward and leeward sensors as well as decrease, being: 1.3 and 2.7 kHz at α = 12°, 1.0 kHz at α = 16° and a minor peak at 0.8 kHz at α = 20°. A minor peak is also detected at 2.0 kHz for α = 12°. In general, as AOA increases, the peaks become broader and less defined than for lower AOA cases.

Figure 12 (Run 165) is a repeat of run 166 with $C_T = 1.97$, but with roll equal to 180°. The results, with the exception of the zero AOA-pairs, are essentially the same as the previous discussion, but the windward sensors are now the leeward sensors, and vice-versa. For instance, TP 2225 and 2216 for α = 20° show an angle of attack affect with the PSD amplitudes split between the windward and leeward sensors. For run 166, TP 2225, the p106, p107 and p108 sensors are windward and thus have a higher amplitude; whereas for run 165, TP 2216, sensors p110 and p111 are windward and have a higher amplitude. Note, the p109 sensor is only very slightly windward or leeward based on these two rolls, regardless of α. Also, the 0° AOA-pair (TP 2211 and 2217) reflect the same trends as seen in the first alpha of zero case for run 166 with a sharp peak at 2.2 kHz and multiple resonance peaks at higher frequency. However, no peak is apparent at 2.0 kHz as for the Run 166 alpha of zero repeat.

Early computational results in Reference 12 calculated expected peak frequencies, by various methods described in the text, to experimental dynamic pressure transducer results for Run 165 and α = 0°. Overall the computations and experimental data are in good agreement, with the computational calculations predicting a dynamic peak frequency to range from 1.7 to 2.1 kHz and the experimental results (including the 0° AOA-pair of Run 166) detect peaks ranging from 2.0 to 2.2 kHz. These peak dynamics are ascribed to ring vortex shedding from the jet plume triple point indicated in Fig. 1.

A continuation of the computational results previously discussed, is given in Ref. 13. Further computational analysis of Run 165 describes the unsteadiness as a periodic oscillation of the triple point shown in Fig. 1 at low AOA. As α increases, the flow unsteadiness becomes less periodic, and finally aperiodic at α = 20°. This trend appears to be reflected in the experimental PSD analysis by how sharp or broad a detected peak appears to be. For the lower AOA cases (α = 0°, ±4° and ±8°) of Run 166 and 165 the peaks are very sharp, distinct, and have a relatively large amplitude. However, as α increases, the peaks become broader and less distinct.

B. Tri-nozzle

The tri-nozzle configuration is shown in Fig. 13. The test conditions are Mach 4.6 freestream flow with 180° roll at α = 0 and $C_T = 0.90$, Schlieren results are not available for these conditions with zero roll. Similar to Fig. 6, the freestream flow is from left to right and the retrorockets can be seen thrusting from the model forebody and penetrating the freestream flow. In this orientation there are two jets on the upper portion (top) of the model and a single jet beneath; the third jet is into the plane of the image, directly behind the jet visible on the upper portion of the model. It is seen that the flow is more unsteady than in the single-nozzle case at the same test conditions. This is most evident in the bow shock directly upstream of the single retrorocket. Unlike the single-nozzle case, this flow does not appear to be symmetric, and the bow shock location is also closer to the model forebody.

Figure 14 (Run 252) is a $C_T = 0.90$ tri-nozzle case with zero roll. For the $\alpha = 0°$ case and repeat (TP 3128 and 3134), a minor peak is evident for most sensors at roughly 0.7 kHz. This same peak at 0.7 kHz is also the most prominent feature for the $\alpha = -8°$, -4° and +4° cases for windward sensors. The exception being two leeward sensors detecting a slight peak at the same frequency ($\alpha = -8°$ sensor p107, $\alpha = +4°$, sensor p109). For $\alpha = 8°$ and 12° the peak migrates to a slightly lower frequency, with the minor peak being most evident for the two windward sensors (p106, p108) and a single leeward sensor (p109), at 0.6 and 0.5 kHz. No peaks are observed at the highest angles of attack, $\alpha = 16°$ and 20°.

Figure 13 – Sample Schlieren result for tri-nozzle at Mach 4.6, $\alpha = 0°$, $\beta = 180°$, and $C_T = 0.90$

Figure 15 (Run 247) is for $C_T = 1.92$ with no roll. Overall there are not many significant peaks evident throughout the alpha sweep. The $\alpha = 0°$ cases (TP 3083 and 3089) register a small peak for all the sensors at 0.2 kHz as well as secondary broad peaks at 1.0 (p107, p111) and 1.2 kHz (p108, p109). The lowest frequency peak appears to be maintained from 0.1 to 0.2 kHz throughout most of the alpha sweep, being evident for $\alpha = -8°$, -4°, +4°, +8° and +20°; although, at the greatest AOA, the peak is only evident for two windward sensors, p106 and p108. Sensor p109, which is the most inboard and in close proximity to a retrorocket, has a peak ranging from 1.2 to 1.3 kHz for the ±4° and ±8° AOA-pairs. For AOA greater than 8° the p109 sensor no longer detects a peak, although sensor p111, which is in close proximity to the top-most jet and on the leeward side, detects a broad peak which increases with AOA from 0.9 to 1.2 kHz.

Overall the tri-nozzle case is more unsteady than for the single-nozzle case at similar C_T, which appears to be reflected by the pressure peak dynamics detected by the sensors. Unlike the single-nozzle case, PSD peaks tend to be at lower frequencies for the tri-nozzle case and peaks observed are typically less defined, being very small and broad. The tri-nozzle case, especially at $C_T = 0.90$, does have some similarities with the single-nozzle $C_T = 0.22$ case. Most notably, the peak detected at 0.7 kHz in the tri-nozzle case is not noticeably affected by the AOA variation for $\alpha = 0°$, ±4°, and ±8°.

C. Quad-nozzle

A sample Schlieren image of the quad-nozzle with $\alpha = 0°$, $C_T = 0.91$ and zero roll in freestream Mach 4.6 flow is shown in Fig. 16. Once again flow is from left to right. The quad-nozzle configuration has 3 peripheral jets and a single central jet. At this roll orientation, f = 0°, two peripheral nozzles are on the upper part of the model forebody, one visible, the second in the plane of the page, and the third is on the lower part of the forebody. Similar to the tri-nozzle configuration, the flow is largely unsteady, most notably seen in the still in the geometry of the bow shock. Further, the symmetry observed for a single central nozzle case does not appear to be present. This single image still implies the quad-nozzle may have a larger shock stand-off than the comparable tri-nozzle case, which is counter-intuitive. However it is not currently apparent whether this is due to a large fluctuation due to the unsteady nature of the flow.

Figure 16 – Sample Schlieren result for quad-nozzle at Mach 4.6, $\alpha = 0°$, $\beta = 0°$, and $C_T = 0.91$

Figure 17 (Run 315) is the quad-nozzle with $C_T = 0.91$ and zero roll. Peaks are readily apparent for the 0° and 4° AOA-pairs (TPs 3631, 3637 and 3630, 3632, respectively) at lower frequencies. The 0° AOA-pair shows good repeatability with a peak at 0.5 kHz for sensor p109, and 0.8 kHz for all other sensors. Peak locations for the

4° AOA-pair also appear to be in the same range, but shifted to a slightly lower frequency with both having peaks detected at 0.5 to 0.6 kHz for all sensors, with the exception of p109. The peak is most prominent and sharp for two sensors located on the windward side for the negative AOA case, p106 and p108. A low-frequency peak is also detected at 0.1 kHz for all but the p109 sensor at $\alpha = -4°$. Very minor peaks are detected at various AOA ($\alpha = -8°$, sensors p110 and p111 at 0.5 kHz, $\alpha = 16°$ and 20°, sensor p109 at 0.3 kHz and 1.0 kHz, respectively), but no discernible peaks for $\alpha = 8°$ and 12°, with the sensors signals looking to be slightly noisy at low frequency.

Figure 18 (Run 307) is another quad-nozzle case at for $C_T = 1.92$ and zero roll. Unlike the lower C_T, this run has many very distinct peaks over a much larger frequency range. The zero AOA-pair (Points 3558 and 3564) has two closely spaced, sharp peaks at 2.2 kHz (sensors p107, p108, p109) and 2.3 kHz (sensors p110, p111). The former peak seems to be present for sensors primarily close to the jet centered on the 120° roll position of the model forebody (as seen in Figure 5), while the latter peak is reflected in sensors closer to the jet centered on the 0° position of the forebody. At higher frequencies the peaks begin to broaden, sensors p109 and p110 have a broad peak at 3.4 kHz and sensor p111 has a broad peak shifted to a slightly higher frequency at 3.6 kHz. A final broad peak appears for the p109 and p111 sensors at 6.8 kHz, which may be a harmonic peak of the 3.4 kHz peak for sensor p109, however the p110 sensor has no detectable peak (harmonic) in this region. The only other peak detected for the zero AOA-pair is a small, sharp peak centered at 4.6 kHz as reported by sensor p107, which could be a harmonic peak. Many interesting dynamics and frequency shifts are observed in the ±4° and ±8° AOA-pairs (Points 3557, 3559 and 3556, 3560, respectively). The negative AOA peaks appear to mirror the sharp peaks observed in the zero AOA-pairs, but are shifted to a lower frequency for windward sensors and a higher frequency for leeward sensors. The -4° AOA has a very sharp peak at 2.1 kHz (sensors p109, p110, p111) and 2.4 kHz (sensors p107, p108 and p109). Note, sensor p109 detects both peaks. Once again, broader peaks are detected at higher frequency and indicated in the Figure. The final negative AOA case, $\alpha = -8°$, has the largest, sharp peak of all cases centered at 1.8 kHz for four sensors (p106, p107, p109 and p111). Two of the sensors are on the windward side near the top center jet, while the other two sensors are on the leeward side near the bottom left jet. There is also a very broad peak at lower frequency for two sensors (p109, p110), and multiple broad peaks at higher frequency for multiple sensors (p106, p107, p108) as indicated. The positive $\alpha = 4°$ and 8° cases have smaller, more broad peaks than the negative-AOA counterparts. Sensors on the windward side (p106, p107, p108) have a large peak that increases from 1.9 kHz to 2.5 kHz as the AOA increases from 4° to 8°; note the p108 peak actually drops out at the higher AOA (also note, the off-set between sensors p106/p108 and p107 is very evident on the plot, however rounding would indicate similar frequencies, thus the plot is labeled to more significant figures). The leeward sensors (p109, p110, and p111) have small peaks centered at 1.1 kHz at +4° and as the AOA increases to 8° the peak frequency increases to 1.2 kHz and two windward sensors develop a peak at that location as well (p107 and p108). For AOA greater than 8° only minor, broad peaks are detected: $\alpha = 12°$ sensors p110, p111 at 0.9 kHz, $\alpha = 16°$ sensor p111 at 1.0 kHz, and $\alpha = 20°$ sensor p106 at 0.3 kHz and p109 at 0.4 kHz.

The quad-nozzle cases were unique with the lower $C_T = 0.91$ case exhibiting trends similar to the tri-nozzle $C_T = 0.90$. The peak frequencies occur under 1 kHz are maintained in the range of 0.5 to 0.8 kHz, and are not very defined, once again being small and broad, indicative of less periodic behavior. However, the $C_T = 1.92$ case exhibits traits similar to the largest C_T discussed for the single-nozzle test cases (Run 165 and Run 166). The primary peaks observed at 2.2 and 2.3 kHz for the zero AOA-pair are very sharply defined, and are roughly equivalent to the peak observed for Runs 165 and 166 $\alpha = 0°$ cases. Also, as AOA increases the peaks become smaller and more broad, essentially less defined, indicating a less periodic unsteady dynamic. This is in agreement with the observation noted in Ref. 13, that the quad-nozzle run 307 exhibits similar periodic behavior to the single-nozzle case.

IV. Conclusion

In summary, high speed forebody pressure data for a 70° sphere-cone blunt body utilizing retropropulsion at a range of supersonic freestream Mach numbers, a range of C_T, and nozzle configurations was tested at the NASA LaRC UPWT to detect possible unsteady effects and trends. The resulting high speed pressure transducer data is analyzed using a MatLab Welch PSD to resolve certain key frequency peaks. Results for a single, tri, and quad-nozzle configuration in freestream Mach 4.6 have been reported for C_T ranging from 0.0 to 2.0 and angle-of-attack (AOA) varying from -8° to +20° in 4-degree increments.

The PSD analysis indicates there are no detectable periodic dynamics in a baseline reference case with no retrorockets. However, there is a slight AOA affect which separates windward from leeward sensors, as the windward sensors have overall larger amplitudes. This trend continues throughout the single central nozzle retrorocket test cases at all C_T. Although, different dynamics were detected as C_T increased. The first thrusting case

discussed, C_T = 0.22, had very few peaks, and the most prominent of the peaks was nearly constant at the same frequency throughout the AOA sweep. The next two cases discussed, C_T = 0.46 and 0.94, had multiple notable peaks for the α = 0° case, and as the angle of attack increased the windward sensor peaks tended to slightly increase in frequency, whereas the leeward peaks decreased in frequency. Peak locations were also similar between the ±4° and ±8° AOA-pairs, but with the windward and leeward sensor amplitudes and peaks swapped. The final single-nozzle test cases discussed were for C_T = 1.97 and had a roll angle of 0° and 180°. Overall, the only observed effect of rolling the model was similar to what was observed for the ±4° and ±8° AOA-pairs at lower C_T; the windward sensors became the leeward sensors and vice-versa. Thus the sensor amplitude and peak frequencies were also swapped, with the exception of sensor p109, which is near the axis of rotation, and is thus wasn't quite windward or leeward. It was also noted that, unlike the previous two smaller C_T cases (0.46 and 0.94), the peak frequency initially decreased from α = 0° to ±4° for the windward sensors while the leeward sensor frequencies slightly increased. For α greater than 4° the windward and leeward sensors tended to report the same peak frequency, which continued to decrease as α increased. Lastly, when compared with computational fluid dynamic results it was found that the shape and size of the peak could be an indication of the periodicity of the unsteady nature of the flow. This correlation is best observed for Run 165 and 166, where the zero AOA-pair is considered to be periodic and has very sharp, distinct peaks. As α increases these peaks shift and have a small amplitude and more broad structure, while the computational results indicate a shift to less periodic behavior, until α = 20° where the behavior is noted to be aperiodic and the power spectral density peak is observed to be very minor and broad.

In general, the tri-nozzle peaks occur at lower frequencies than observed in the single-nozzle cases, and the peaks are typically small and broad, which could be an indicator of the aperiodic nature of the unsteady flow. Although, the tri-nozzle PSD analysis does have some similarities with the lowest thrust coefficient for the single-nozzle case at both C_T = 0.90 and 1.92. Notably, the peak frequency evident at the 0° AOA-pair does not tend to migrate with increasing or decreasing AOA as observed in other runs. For instance, the lower thrust case has a peak at 0.7 kHz that is picked up by most sensors, but as alpha varies the peak remains while the sensors detecting the peak may change. Overall, the relationship between sensor location on the forebody and AOA-effects are not clear for the tri-nozzle case. Peaks are detected at similar frequencies by both windward and leeward sensors, as well as sensors close to retrorocket jets and sensors placed between jets.

Two completely different types of dynamics were detected in the two thrust coefficients discussed for the quad-nozzle tests. The first run, C_T = 0.91, was similar to the tri-nozzle case with producing minor, broad peaks throughout the alpha sweep. Although, it was observed the peaks may be dependent on sensor location, as the primary peak for the 0° and 4° AOA-pairs were detected for all the peripheral sensors, whereas a different peak or no peak was detected by the sensor furthest from the forebody peripheral. The larger thrust case, C_T = 1.92, had dynamics more similar to the largest thrust coefficient for the single-nozzle run with the windward sensors shifting to lower frequency and leeward sensors shift slightly to higher frequencies for the 4° AOA-pair. However, similar to the single-nozzle case, the windward and leeward sensor peaks begin to match-up again for the 8° AOA-pair. Finally, as alpha increases to 12° and greater, the peak dynamics begin to be less pronounced, possibly indicating a shift to less periodic behavior as observed in the single-nozzle case.

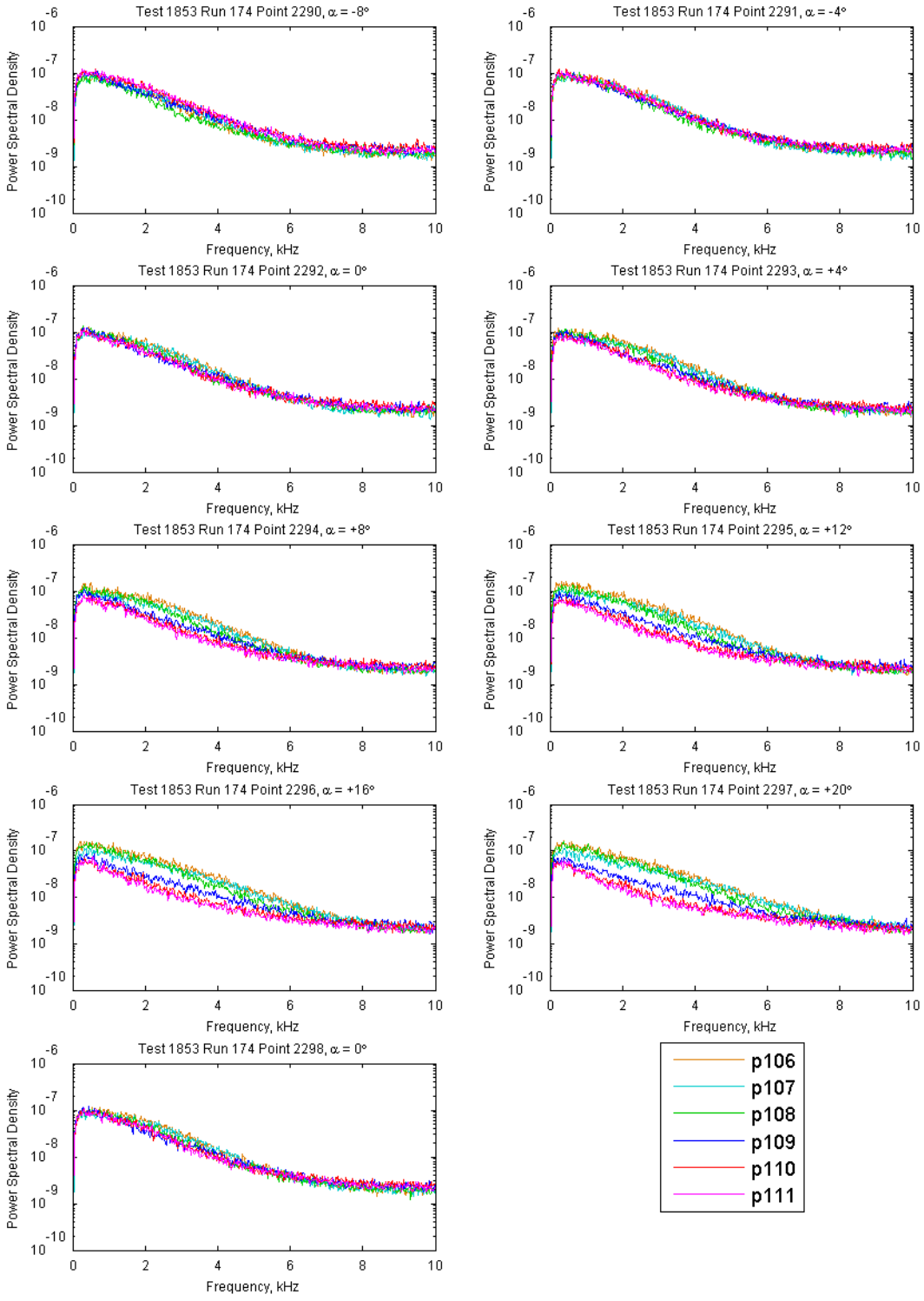

Figure 7 – Run 174, Background test case C_T = 0.00, Roll = 0

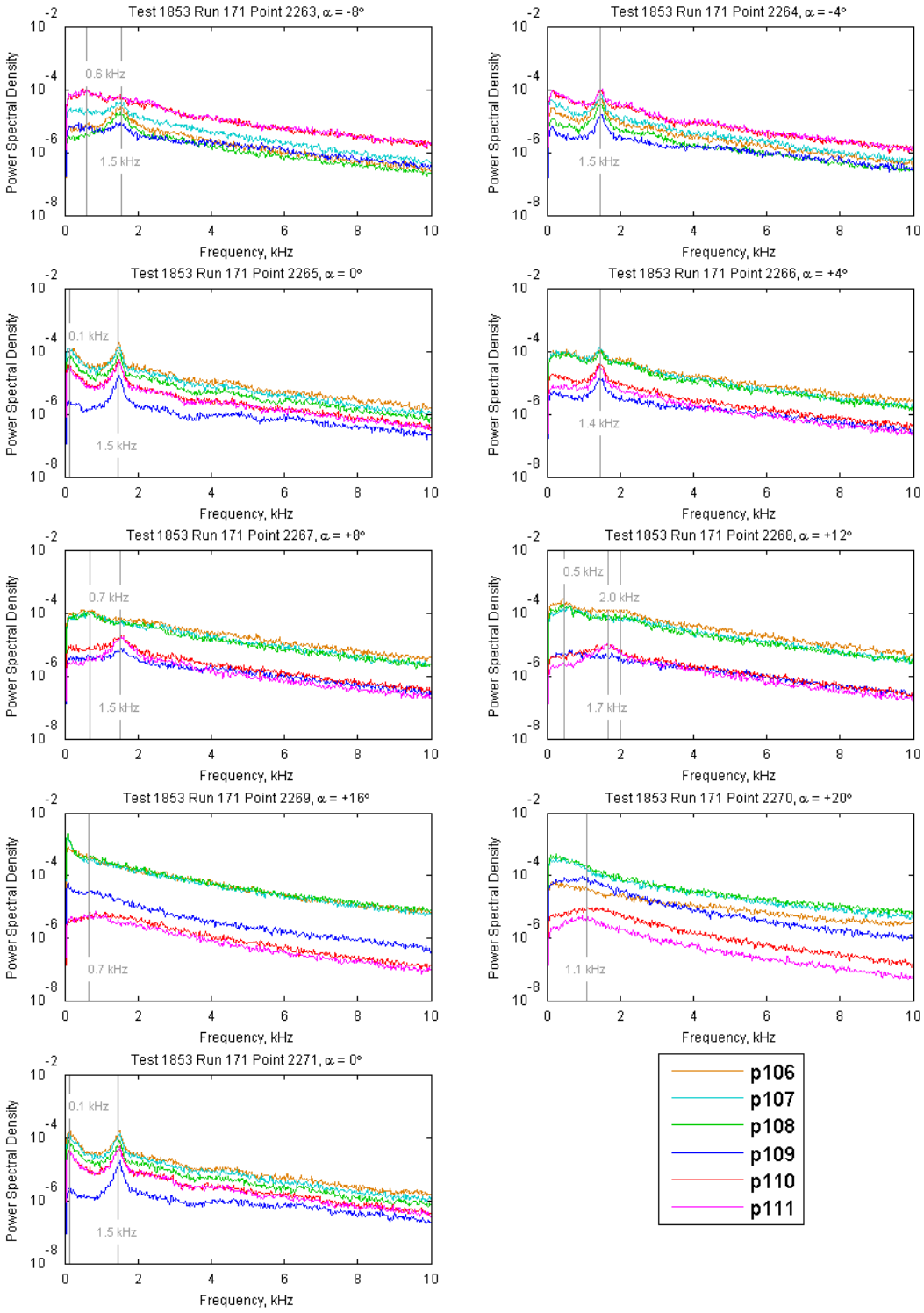

Figure 8 – Run 171, $M_\infty = 4.6$, $C_T = 0.22$, Roll = 0

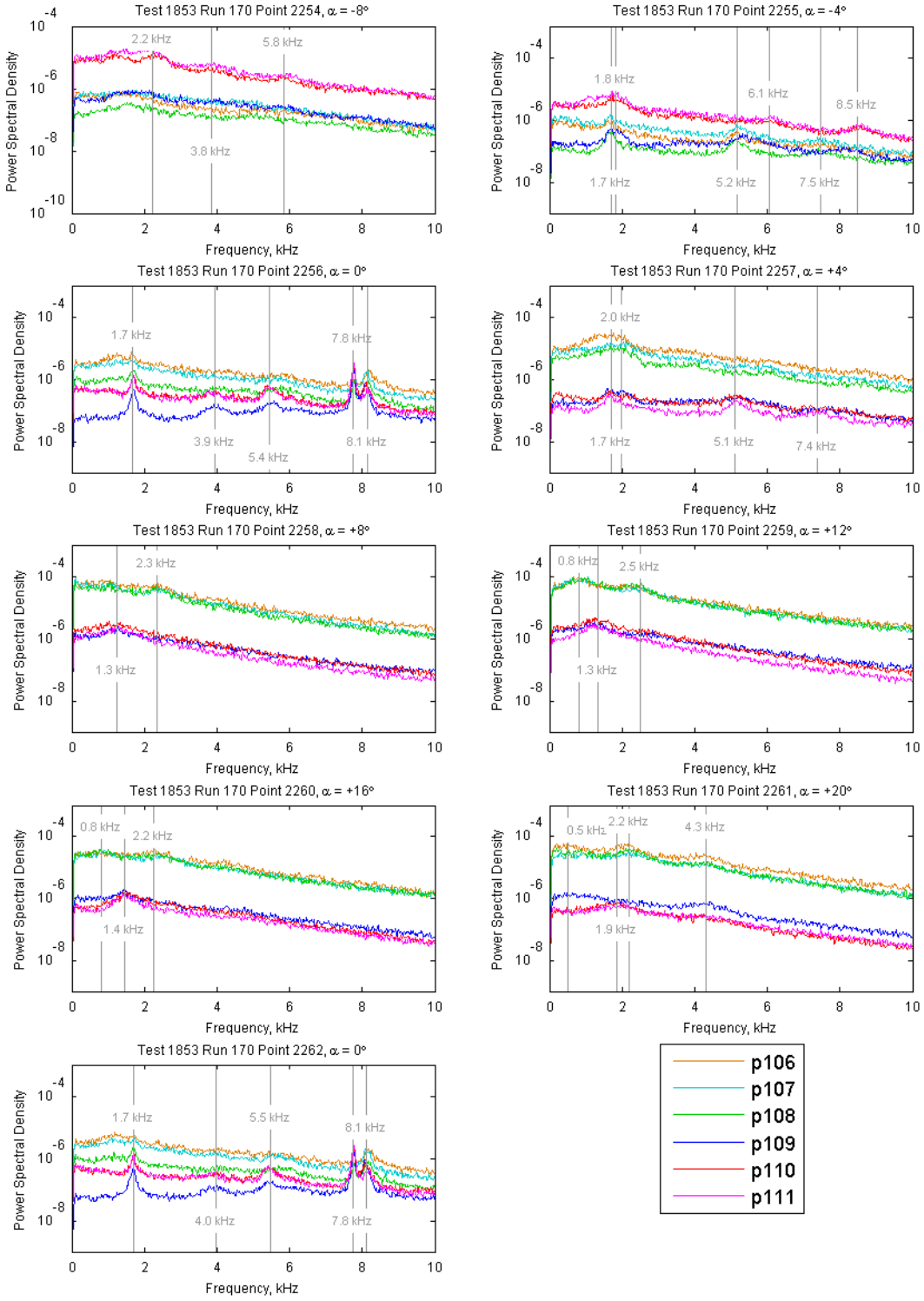

Figure 9 – Run 170, $M_\infty = 4.6$, $C_T = 0.46$, Roll = 0

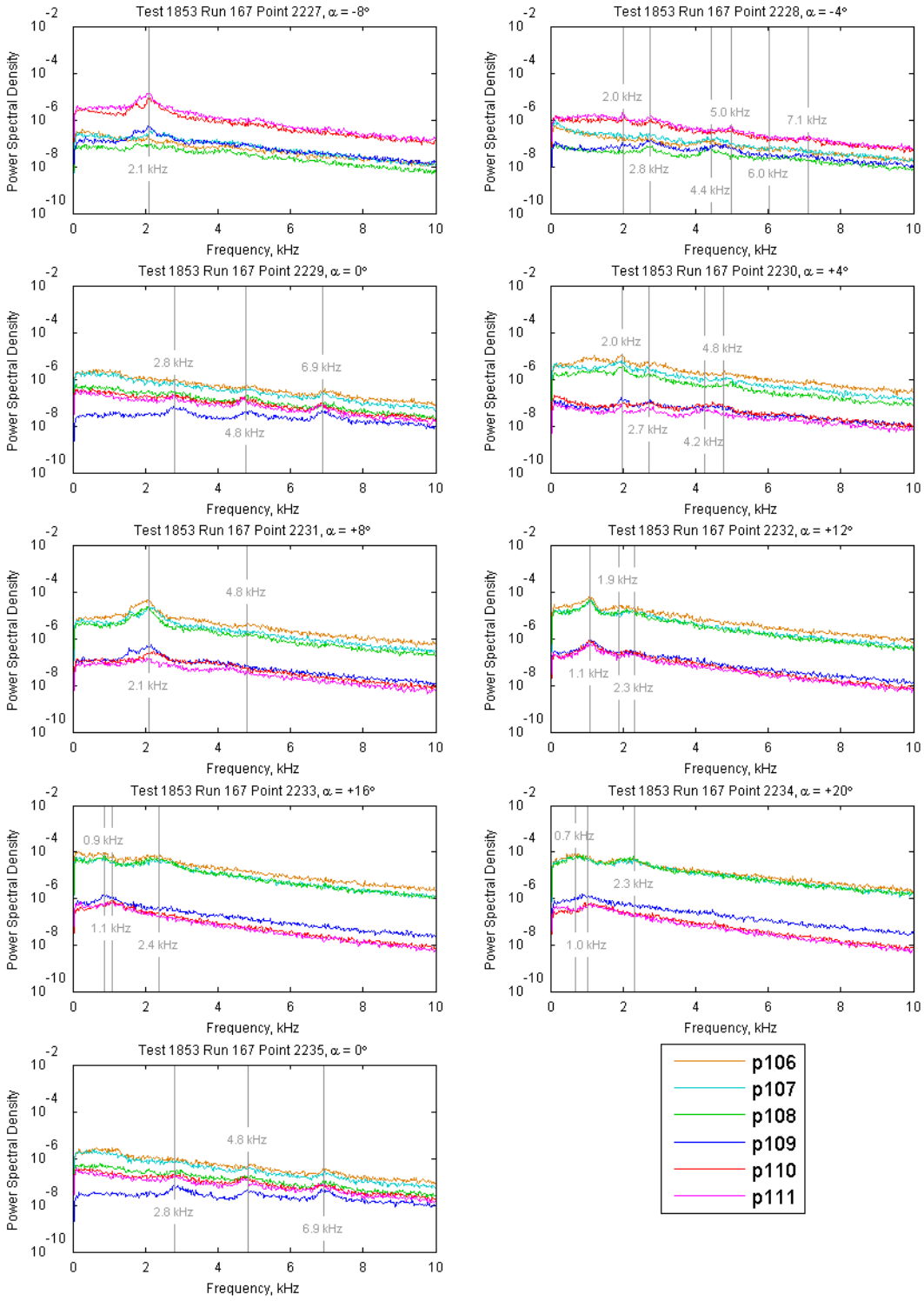

Figure 10 – Run 167, $M_\infty = 4.6$, $C_T = 0.94$, Roll = 0

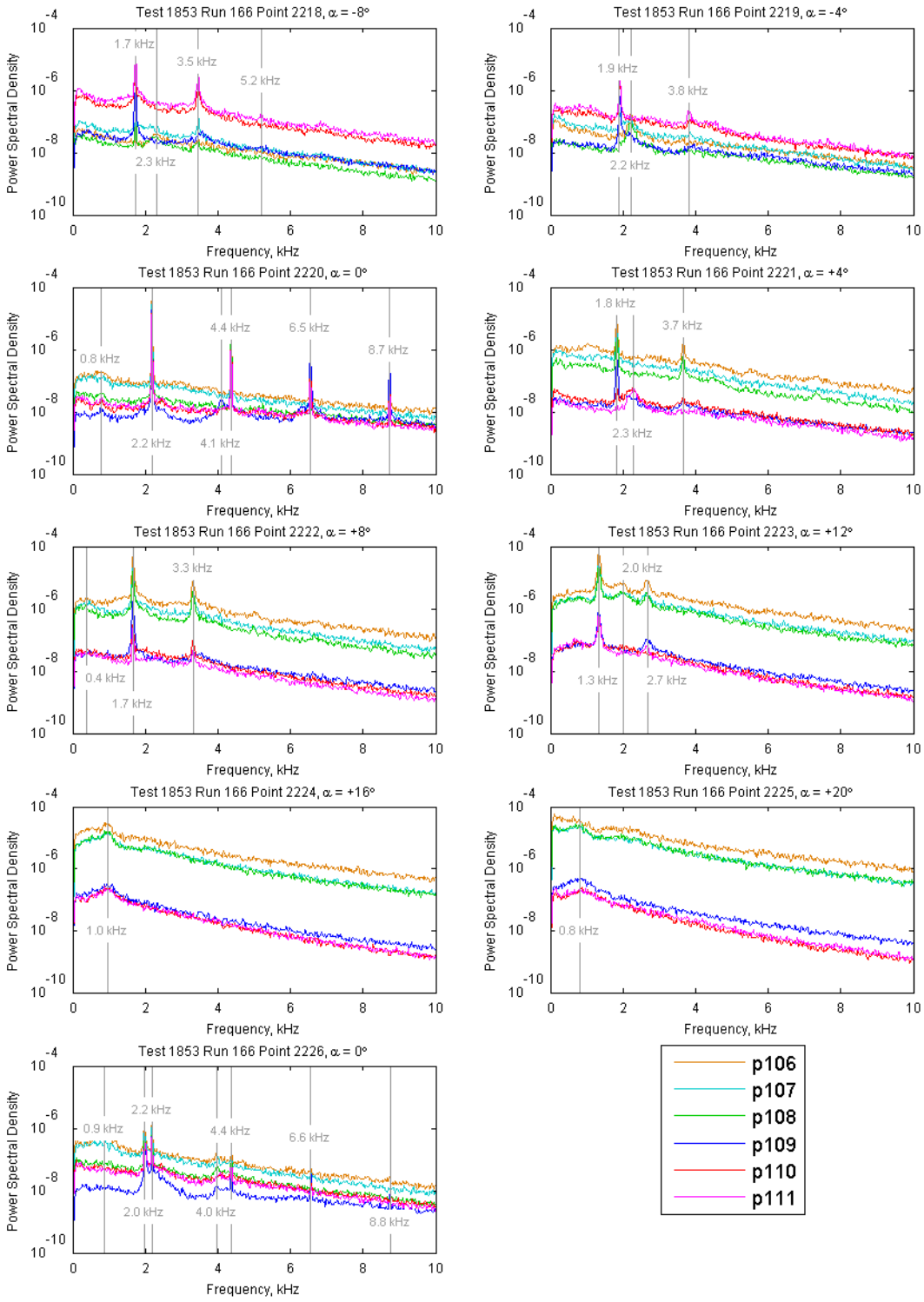

Figure 11 – Run 166, $M_\infty = 4.6$, $C_T = 1.97$, Roll = 0

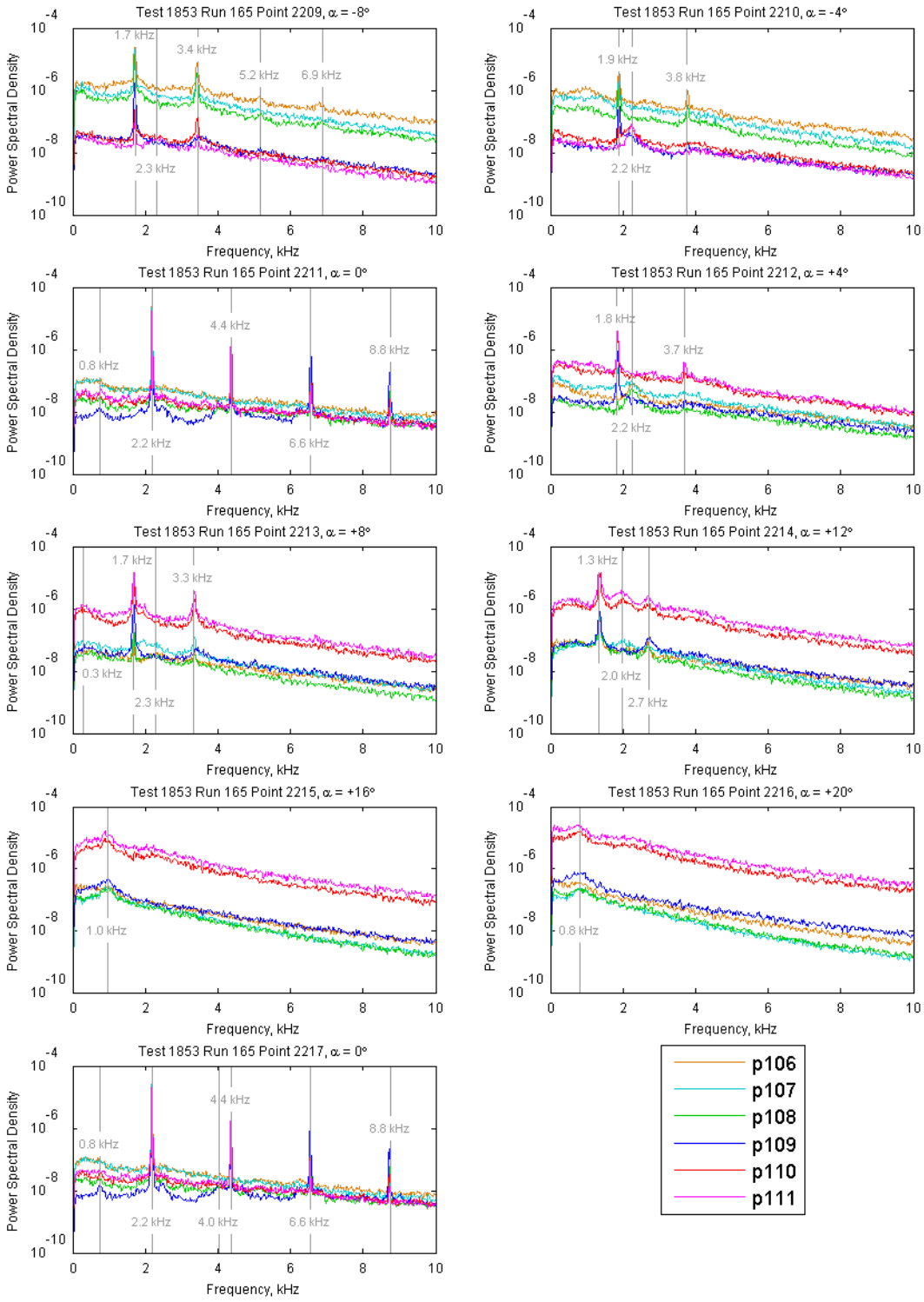

Figure 12 – Run 165, $M_\infty = 4.6$, $C_T = 1.97$, Roll = 180°

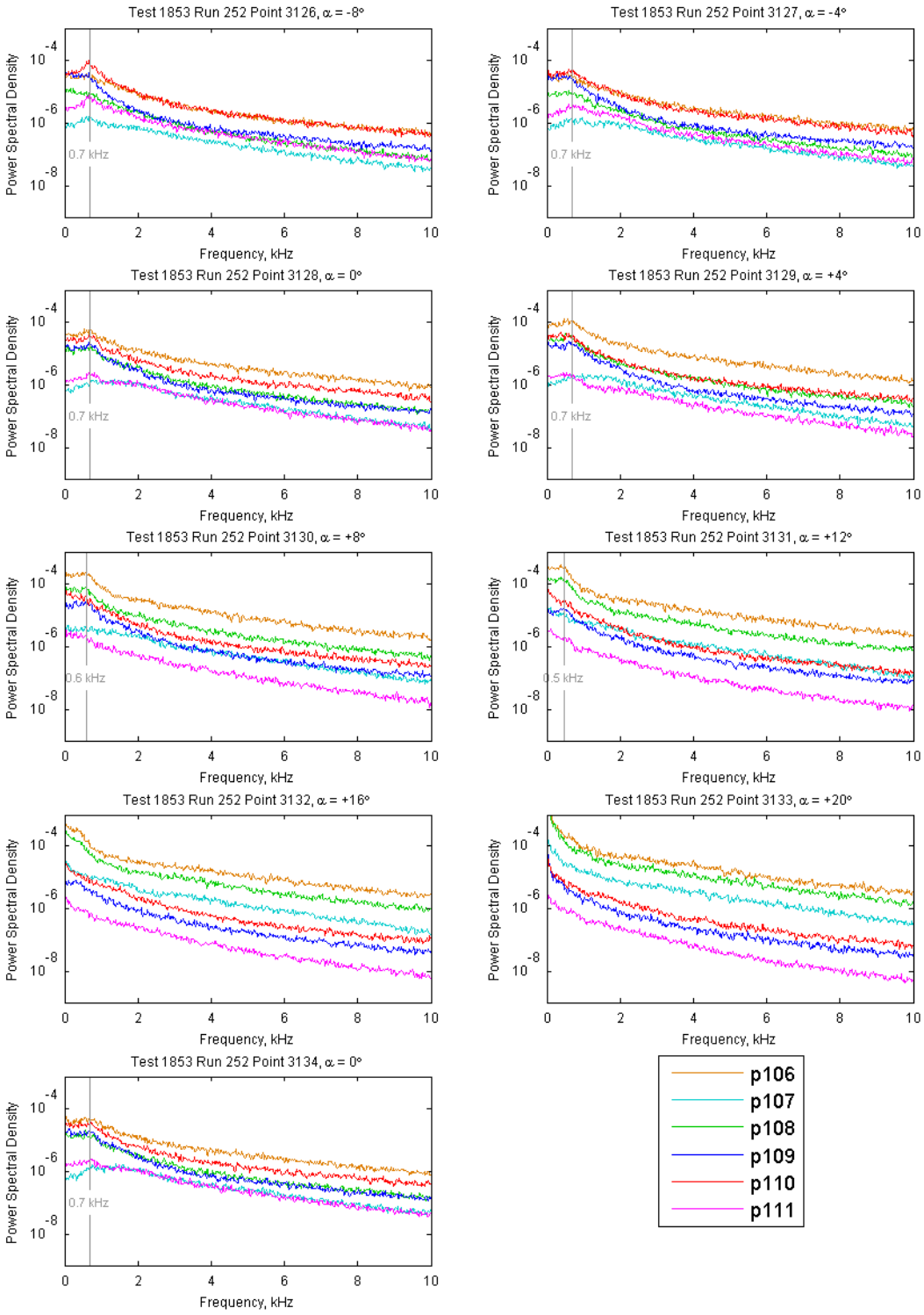

Figure 14 – Run 252, $M_\infty = 4.6$, $C_T = 0.90$, Roll = 0

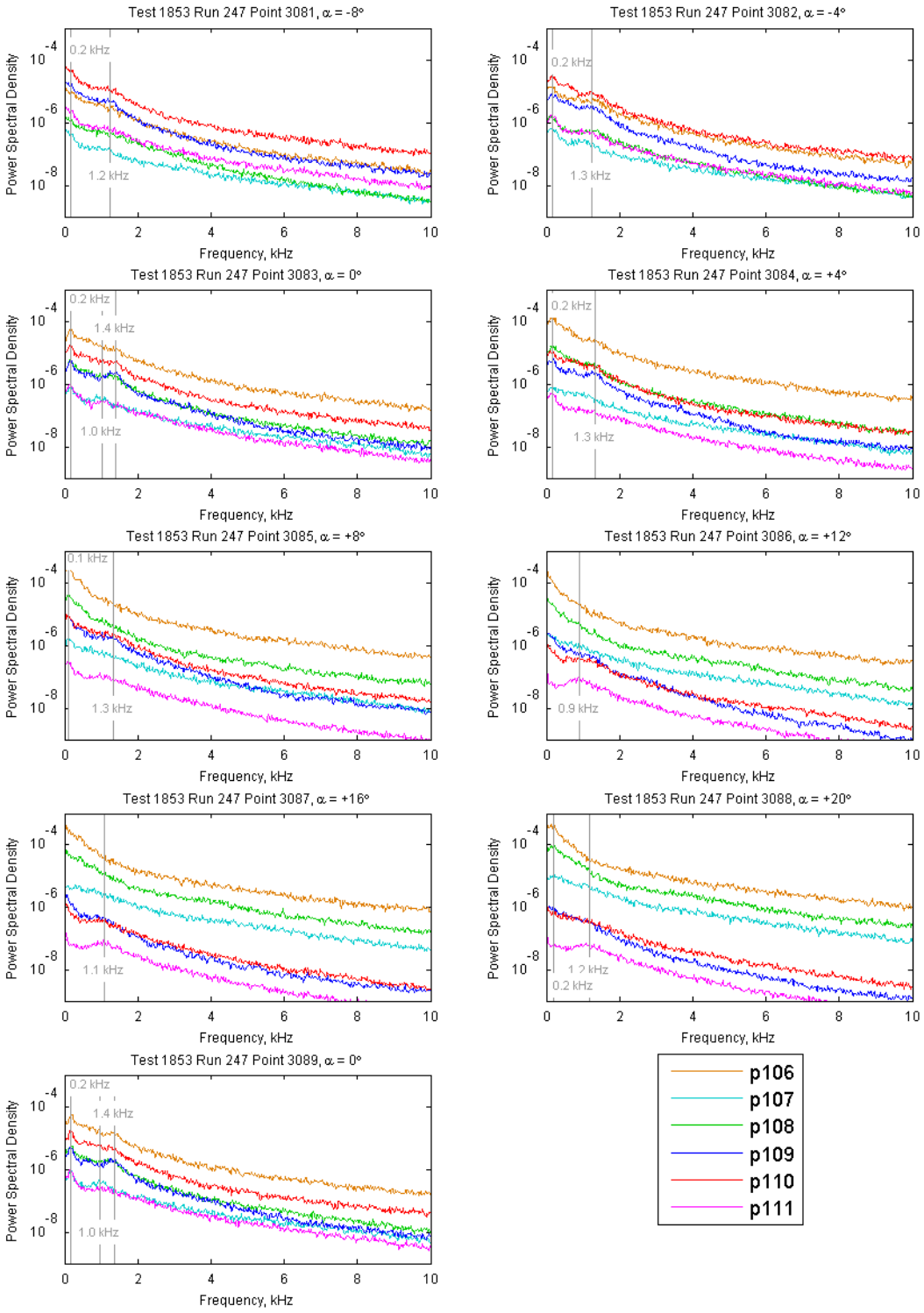

Figure 15 – Run 247, $M_\infty = 4.6$, $C_T = 1.92$, Roll = 0

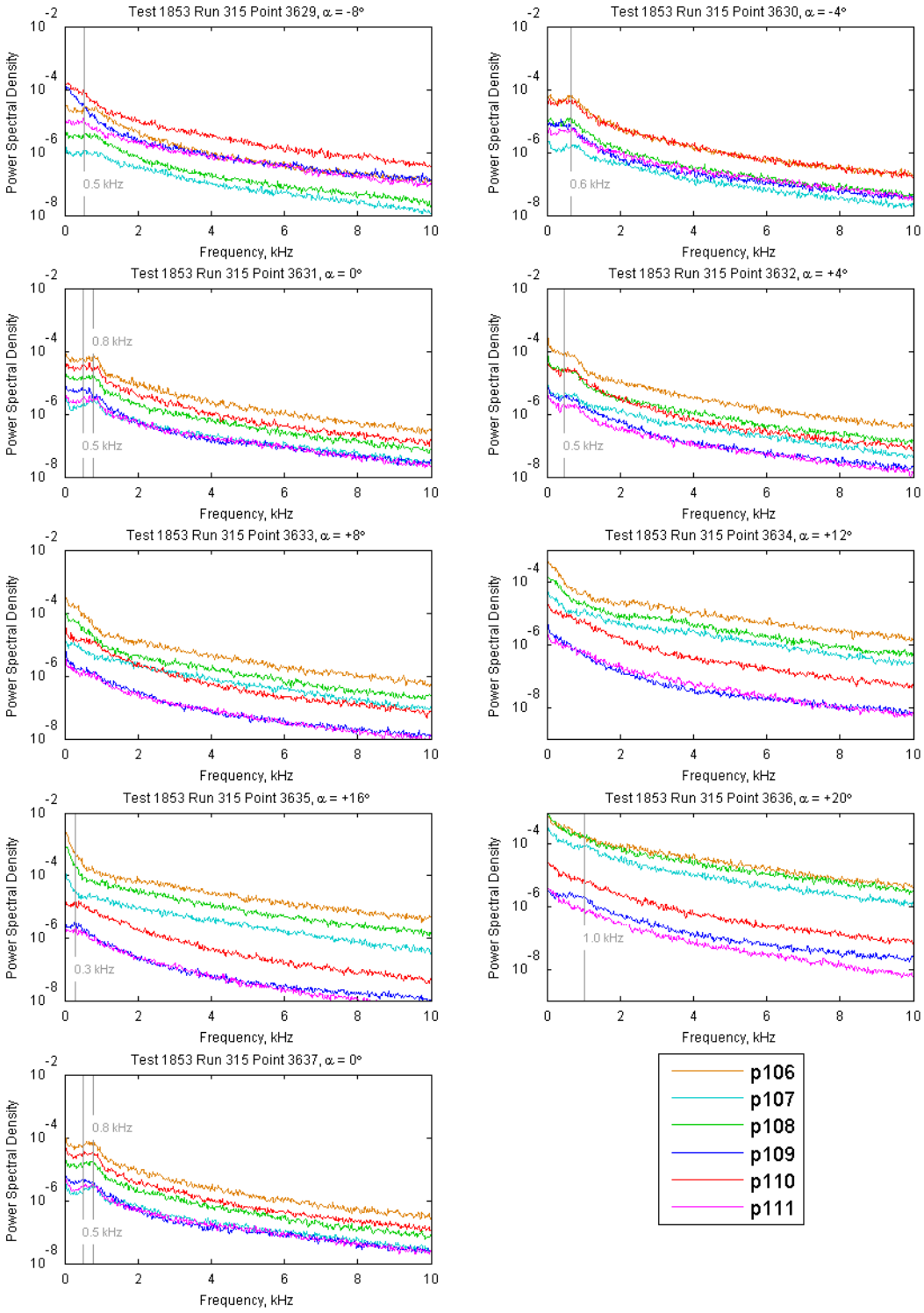

Figure 17 – Run 315, $M_\infty = 4.6$, $C_T = 0.91$, Roll = 0

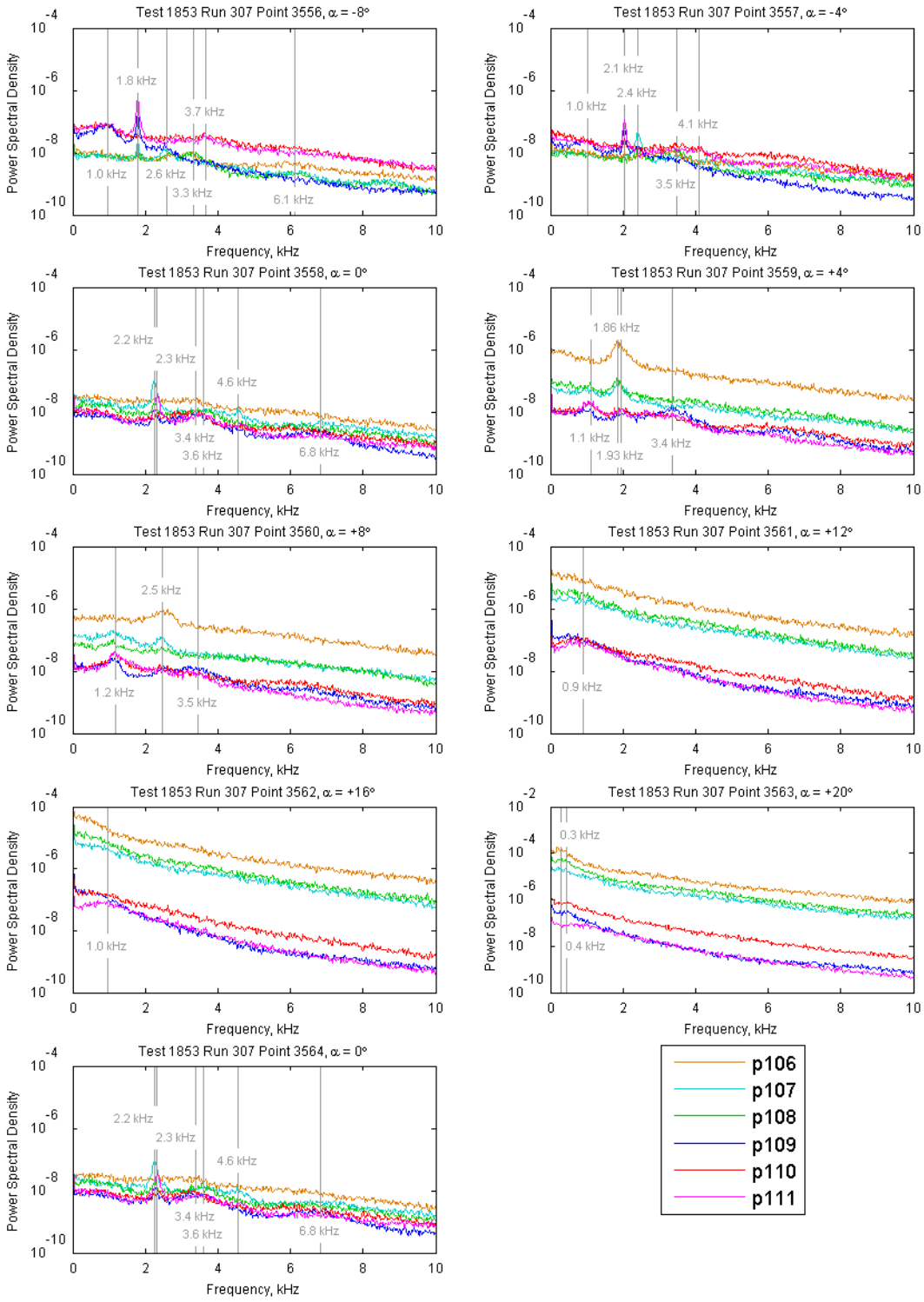

Figure 18 – Run 307, $M_\infty = 4.6$, $C_T = 1.92$, Roll = 0

References

[1] Braun, R. D., and Manning, R. M., "Mars Exploration Entry, Descent, and Landing Challenges," *Journal of Spacecraft and Rockets*, Vol. 44, No. 2, 2007, pp. 310–323.

[2] Zang, T. A., and Munk, M. M., et al., "Entry, Descent and Landing Systems Analysis Study: Phase 1 Report," NASA TM 2010-216720, July 2010.

[3] Steinfeldt, B. A., Theisinger, J. E., Korzun, A. M., Clark, I. G., Grant, M. J., and Braun, R. D., "High Mass Mars Entry, Descent, and Landing Architecture Assessment," AIAA Paper 2009-6684, Sept. 2009.

[4] Edquist, K. T., Dyakonov, A. A., Korzun, A. M., Shidner, J. D., Studak, J. W., Tigges, M. A., Kipp, D. M., Prakash, R., Trumble, K. A., Dupzyk, I. C., "Development of Supersonic Retro-Propulsion for Future Mars Entry, Descent, and Landing Systems," AIAA Paper 2010-5046, June 2010.

[5] Korzun, A. M., and Braun, R. D., "Performance Characterization of Supersonic Retropropulsion for High-Mass Mars Entry Systems," *Journal of Spacecraft and Rockets*, Vol. 47, No. 5, pp. 836-848, 2010.

[6] Jarvinen, P. O., and Adams, R. H., "The Aerodynamic Characteristics of Large Angled Cones with Retrorockets," NASA CR NAS 7-576, Feb. 1970.

[7] Keyes, J.W. and Hefner, J.N., "Effect of Forward-Facing Jets on Aerodynamic Characteristics of Blunt Configurations at Mach 6," Journal of Spacecraft and Rockets, Vol. 4, No. 4, 1967, pp. 533-534.

[8] Trumble, K. A., Schauerhamer, D. G., Kleb, W. L., Carlson, JR., Buning, P. G., Edquist, K. T., and Barnhardt, M. D., "An Initial Assessment of Navier-Stokes Codes Applied to Supersonic Retro-Propulsion," AIAA Paper 2010-5047, June 2010.

[9] Rhode, M.N. and Oberkampf, W.L., "Estimation of Uncertainty for a Supersonic Retro-Propulsion Model Validation Experiment in a Wind Tunnel," 42nd AIAA Fluid Dynamics Conference, New Orlenas, LA, June 2012 (submitted for publication).

[10] Berry, S.A., Laws, C.T., Kleb, W.L., Rhode, M.N., Spells, C., Mccrea, A.C., Trumble, K.A., Schauerhamer, D.G., Oberkampf, W.L., "Supersonic Retro-Propulsion Experimental Design for Computational Fluid Dynamics Model Validation," IEEE Aerospace Conference Paper No.1499, March 2011.

[11] Berry, S.A., Rhode, M.N., Edquist, K.T., and Player, C.J., "Supersonic Retropropulsion Experimental Results from the NASA Langley Unitary Plan Wind Tunnel," AIAA Paper 2011-3489, Jun. 2011.

[12] Kleb, B., Schauerhamer, D.G., Trumble, K.A., Sozer, E., Barnhardt, M., Carlson, J.R., and Edquist, K.T., "Toward Supersonic Retropropulsion CFD Validation," AIAA Paper 2011-3490, Jun. 2011.

[13] Schauerhamer, D.G., Trumble, K.A., Kleb, B., Carlson, J.R., and Edquist, K.T., "Continuing Validation of Computational Fluid Dynamics for Supersonic Retropropulsion," AIAA Paper 2012-0864, Jan. 2012.